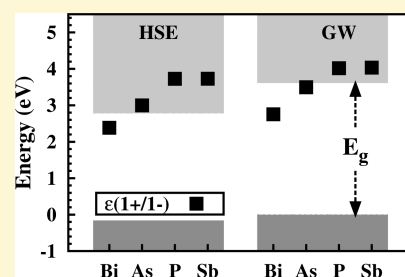


Multivalency of Group 15 Dopants in SnO₂

Haowei Peng,* John D. Perkins, and Stephan Lany*

National Renewable Energy Laboratory, Golden, Colorado 80401, United States

ABSTRACT: The multivalent behavior of group 15 elements P, As, Sb, and Bi, on the cation site in SnO₂ has been studied via first-principles calculations. Through accurate calculation of the energy position of the defect transition energy levels with respect to the host conduction band minimum using a combination of hybrid functional and GW calculations, we found that As and Bi will change their oxidation state from +5 to +3 when the Fermi level approaches the conduction band minimum, while P and Sb will stay in the +5 state until the Fermi level rises to an energy well above the conduction band minimum. The change of the oxidation state is associated with the occupation of an electron-compensating defect state resulting from the antibonding s-p hybridization between the group 15 dopant and the ligands. Thus, only P and Sb are good electron-dopants (donors). As is a borderline case allowing only limited *n*-type doping, whereas Bi is a deep defect that pins the Fermi level within the band gap and causes insulating behavior. We discuss the chemical trends with the atomic energy of the valence s state and the ionic radii of the dopants.



INTRODUCTION

Doping is one of the essential processes for semiconductor applications. For electron (*n*-type) doping, we usually look in the periodic table of elements for donor dopants in the column to the right of the constituent elements. For example, we choose P as a donor dopant for Si, Ga for ZnO, Sn for In₂O₃, and F and Sb for SnO₂. However, unexpected phenomena may occur when multivalent elements are involved, whose oxidation state depends on the chemical environment. This kind of multivalent behavior is common in transition-metal elements due to their open d-shell and is related to the small-polaron hopping conduction in some transition-metal semiconductors such as rocksalt MnO and hematite Fe₂O₃.^{1–3} As for the main-group elements, the heavy p-block elements can also show such multivalent behavior. For example, in BaBiO₃, Bi is formally in the oxidation state of +4 but actually possesses the oxidation states of +3 and +5, with the BiO₆ octahedra expanding out and contracting in, respectively.⁴ As another example, both Sb³⁺ and Sb⁵⁺ have been detected by Mössbauer spectroscopy in Sb-doped BiSnO₃,⁵ which is closely related to the subject of this study, group 15 doping in SnO₂.

SnO₂ with anion-site F-doping (FTO) is a widely used *n*-type transparent conducting oxide (TCO), which has been commercially available for a long time.⁶ Compared to the approach of anion-site doping, cation-site incorporation allows a wider range of growth techniques and therefore may lead to cost reduction as well as enhanced performance.⁶ In this context, group 15 elements, including P, As, and Sb, were proposed as cation-site shallow donor dopants in SnO₂, with the assumption that they incorporate in the +5 oxidation state.⁷ Indeed, cation-site group 15 doping of SnO₂ has been considered for several decades,^{8–15} although it was believed that anion-site doping is preferred for such a relatively covalent oxide to create shallow donor levels thanks to a weaker perturbation to the conduction band.¹⁶ Among these group 15

elements, Sb has been successfully used to achieve high *n*-type charge carrier concentrations in SnO₂ for TCO applications.^{11–15} However, Bi doping was found to increase the electrical resistivity of SnO₂ thin films by 3–4 orders of magnitude,^{17,18} leading to insulating behavior. A similar compensation effect exists also in β-PbO₂, where a metal-to-nonmetal transition occurs upon around 5% Bi-doping.¹⁹ As-doping was found to be effective only at low doping levels, with an anomalous feature that the carrier concentration first increases and then decreases with the dopant content until saturation.¹⁰ These experimental observations are not easily explained by the assumed +5 oxidation state of these group 15 dopants.⁷ Therefore, considering the implications of the multivalence of the group 15 elements can shed light on these puzzling phenomena. The direct experimental comparison of the multivalent nature of the different dopants is rather challenging due to the convolution of different effects arising from use of different growth methods, different dopant solubilities, grain boundary effects, or the coexistence of secondary phases. For example, both the absence and existence of Sb³⁺ in Sb-doped SnO₂ have been reported based on Mössbauer spectroscopy from different groups.^{20–22} Hence, theoretical investigation of the intrinsic multivalent behavior of these dopants is highly desirable.

Theoretically, the multivalent behavior can be studied within the framework of first-principles defect theory.²³ Within the supercell approach, the defect formation energy is a function of Fermi level, with the slope equal to its charge state *q*,

$$\Delta H_{D,q}(E_F, \mu) = E_{D,q} - E_H + q(E_V + E_F) - \mu_X + \mu_{Sn} \quad (1)$$

Received: July 3, 2014

Revised: August 4, 2014

Published: August 6, 2014

where $E_{D,q}$ and E_H are the total energies of the supercells with and without the defect, respectively; μ_X and μ_{Sn} are the elemental chemical potentials of the group 15 dopant X and Sn, respectively; E_V is the energy of the host valence band maximum (VBM); E_F is the Fermi level with respect to E_V . Consequently, the defect transition energy level $\epsilon(q/q')$ between charge states q and q' of the defect D is defined as

$$\epsilon(q/q') = [\Delta H_{D,q}(0, \mu) - \Delta H_{D,q'}(0, \mu)] / (q - q') \quad (2)$$

In Figure 1, we plot schematically the defect formation energies as a function of the Fermi level, for charge states of $q =$

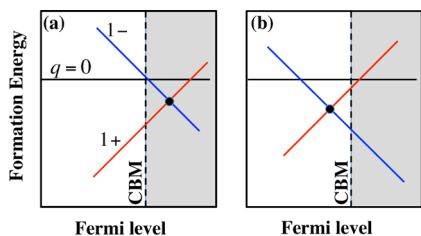


Figure 1. Schematic diagrams of defect formation energy as a function of Fermi level. In case a, the transition energy level $\epsilon(1+/1-)$ is above the conduction band minimum (CBM), and the dopant is a good electron donor; while in case b, when the Fermi level is higher than $\epsilon(1+/1-)$, the dopant becomes an electron-compensator.

$1+$, $q = 0$, and $q = 1-$, which corresponds to the cases where the group 15 dopants are in the +5, +4, and +3 oxidation states, respectively. As we will discuss in more detail below, the group 15 dopants cause a doubly degenerate defect state that is occupied with 0, 1, and 2 electrons for the respective charge/oxidation states. Note that a $q = 0$ state can also occur in the +5 oxidation state when the electron occupies a shallow, effective-mass like “perturbed host state,” but we are here more interested in the “defect-localized state”²⁴ that is caused by the multivalent behavior of the dopants. The defect transition energy level between $q = 1+$ and $1-$, $\epsilon(1+/1-)$, indicates the Fermi level at which the dopant changes its oxidation number between +5 and +3 (see Figure 1). Specifically, if this transition energy level is high in the conduction band as shown in Figure 1a, such a multivalent behavior will be suppressed and high n -type doping levels can be sustained without a change of the oxidation state. However, if the transition energy level is below the host conduction band minimum (CBM) as shown in Figure 1b, an increasing fraction of the group 15 elements will assume the +3 state as the Fermi level approaches the CBM. Since the reduction of the oxidation state consumes 2 electrons, the free carrier density will be limited by the multivalent nature of the dopant in this case.

Another quantity related to the doping behavior is the effective electron interaction U , which is defined as the energy cost to decompose two charge-neutral defects into one in $q = 1-$ and another in $q = 1+$, and can be written as

$$U = \epsilon(0/1-) - \epsilon(1+/0) \quad (3)$$

If the system is a negative- U system²⁵ as shown in Figure 1a and b, the charge neutral state is not stable, and then the doping efficiency is determined by the transition energy level $\epsilon(1+/1-)$, instead of $\epsilon(1+/0)$, which otherwise determines the ionization energy of more conventional donor dopants that are not multivalent. Since +3 and +5 are the prevalent oxidation states of the group 15 elements, one expects that these dopants

will tend to be negative- U systems. Below, we will confirm that all the group 15 dopants are indeed negative- U systems.

COMPUTATIONAL METHODOLOGY

The main interest of the present work, i.e., the doping behavior of the group 15 donors in SnO_2 , depends on the exact position of the defect transition energy level $\epsilon(1+/1-)$, relative to the CBM. However, in density functional theory (DFT) calculations with local or semilocal exchange-correlation functionals, the band gap is severely underestimated, and the conduction band is usually too low in energy. Considering that deep defect levels often align with a constant potential reference, rather than one of the band-edge energies,²⁶ this shortcoming implies that the transition level will lie too high compared to the CBM. An improved description can be obtained by using hybrid functionals,^{27–29} but without empirical parameter adjustment, the band gap is still not accurate enough for the present purpose. Furthermore, since the individual band-edge energies (VBM and CBM) need to be accurate,^{26,30} the hybrid functional parameter adjustment of the band gap alone might not be sufficient. Therefore, we start from the Heyd–Scuseria–Ernzerhof (HSE06)²⁹ hybrid functional and then employ an approach^{31,32} to include GW³³ quasiparticle energy corrections to both the band edge energies and the defect transition level.

All calculations were performed within the framework of the projector augmented wave (PAW) method^{34,35} using the VASP code^{35–37} and pseudopotential data sets for GW-type calculations. The defects were modeled by replacing one Sn atom by the respective group 15 atom in a 72-atom $2 \times 2 \times 3$ supercell, and a $2 \times 2 \times 2$ kmesh was used for Brillouin zone sampling. The HSE06 hybrid functional was used with the standard mixing parameter of 0.25,²⁹ and all equilibrium structures have been relaxed with this functional until the residual forces were smaller than 0.02 eV/Å. During the GW calculations, the initial HSE06 eigenfunctions were kept fixed, but the eigenvalues were iterated to self-consistency. Image charge corrections in the case of charged supercells have been applied for both total energies and quasi-particle energy levels, and the potential alignment was done based on the averaged electrostatic potential.^{32,38}

Within the procedure of the combined DFT+GW approach,^{31,32} the defect transition energy [cf. eq 2] between the initial and final defect charge states q' and q (their respective equilibrium atomic configurations denoted as $R_{q'}$ and R_q) is calculated as the sum of the vertical transition energy and the relaxation energy,

$$\epsilon(q/q') = \epsilon^O(q/q'; R_{q'}) + \epsilon^R(q; R_q \rightarrow R_{q'}) \quad (4)$$

Here, the vertical excitation energies are determined from the GW quasi-particle energy of the defect states, and the atomic geometry and relaxation energies are determined from total energy calculations in the HSE06 hybrid functional. This approach requires well-defined defect states (quasi-particle energy states) within the band gap for the vertical excitations.

Figure 2a shows schematically the path in the configuration coordinate diagram from the initial $q = 1-$ charge state (corresponding to the +3 oxidation state) to the fully ionized $q = 1+$ state (corresponding to the +5 oxidation state). First, we determined the vertical transition energy E_1 from $q = 1-$ to $q = 0$. Particle conservation requires defining a reservoir energy of the electron removed from the defect state, which is taken as the CBM (i.e., in the representation of Figure 1, the Fermi level is set to the CBM energy). Second, we calculated in the $q = 0$ state the energy gain E_2 for relaxation to the new equilibrium structure. The thermodynamic transition level is then obtained as $\epsilon(0/1-) = E_1 + E_2$. In a similar way, we obtained the second transition level $\epsilon(1+/0) = E_3 + E_4$, (cf. Figure 2a), and the negative- U transition is obtained as $\epsilon(1+/1-) = 1/2 [\epsilon(1+/0) + \epsilon(0/1-)]$.

For some of the group 15 dopants, the compensating +3 oxidation state is rather unstable, which is beneficial for electron doping but complicates the computational description of these states. Particularly, due to the negative- U behavior, the $q = 0$ charge state lies even higher in energy than the compensating $q = 1-$ state for Fermi levels below

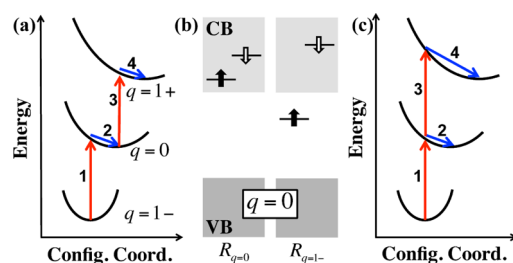


Figure 2. (a) Configuration coordinate diagram illustrating the vertical transition energies E_1 and E_3 (determined from the GW quasi-particle energies of the defect state) and the relaxation energies E_2 and E_4 (determined HSE06 total-energy calculations). (b) Schematic illustration of the defect single-particle energy states for P_{Sn} , As_{Sn} , and Sb_{Sn} in the charge-neutral $q = 0$ state, when the structure is relaxed (left) and when the structure is constrained to the initial $q = 1-$ state (right). (c) Alternate path in the configuration coordinate diagram used to determine the transition levels for these dopants.

the CBM (cf. Figure 1), and except for the case of Bi, the condition of a well-defined defect state inside the gap is not fulfilled for $q = 0$ if the structure is allowed to relax. As illustrated schematically in Figure 2b (applying to the cases of P-, As- and Sb-doping) the occupied defect state in the majority-spin channel lies above the CBM in the ground state structure of $q = 0$ ($R_{q=0}$). In this case, there is an electronic “spillover” from the defect state into the conduction band, leading to a situation that corresponds rather to a $q = 1+$ state with an electron at the CBM than to the true $q = 0$ state. However, a well-defined gap state for $q = 0$ is maintained in the structure of the initial $q = 1-$ state ($R_{q=1-}$ in Figure 2b). Thus, for the vertical transition energy calculated in GW, the problem can be circumvented by determining the second vertical transition (E_3) in the constrained structure of the $q = 1-$ state, as shown in Figure 2c. In order to calculate an accurate relaxation energy E_2 , we found a solution for the charge-neutral defects in the spirit of “constrained-DFT”.³⁹ First, we fixed the total magnetic moment to $1 \mu_B$ to avoid a charge transfer from the majority-spin defect state to the minority-spin conduction-band-derived state; then fixed the occupation to 1 for the majority-spin defect state even it is higher in energy than other conduction-band-derived states to avoid charge transfer within the same spin channel. For P-, As-, and Sb-doping, the transition levels are then determined using an alternate path in the configuration coordinate diagram as shown in Figure 2c. In these cases, the $(1+/0)$ transition is obtained as $\epsilon(1+/0) = E_3 + E_4 - E_2$. We tested this procedure also for Bi_{Sn} and found a difference smaller than 0.02 eV compared to that of the path shown in Figure 2a.

In the case of for Sb_{Sn} , the situation of a defect state above the CBM occurs already in the $q = 1-$ state, which indicates that the compensating +3 oxidation state is very unstable for this dopant. In order to obtain nevertheless a reasonable structural model for this case, we determined the local defect configuration, i.e., the atomic coordinates of the SbO_6 octahedron, in a Hartree–Fock (HF) calculation with 100% of the Fock exchange, where the charge transfer from the defect state into the conduction band is suppressed. The resulting structure has a longer Sb–O bond length, allowing for the Sb-s defect state located within the HSE band gap. In essence, we use these constrained-DFT-like procedures to ensure the one-to-one correspondence between the defect charge state and the oxidation state of the dopant.

RESULTS AND DISCUSSION

Theory Results for Undoped SnO_2 . SnO_2 crystallizes in the rutile structure. In Table 1, we compare the lattice parameters, band gap, and static dielectric constants along and perpendicular to the c axis, as obtained in the HSE06 calculation with the respective experimental data.⁴⁰ The difference for the lattice parameters is smaller than 1%. On the basis of the HSE wave functions, the GW calculation shifts

Table 1. Lattice Parameters, Band Gap, and Static Dielectric Constants from Hybrid Density Functional Theory Calculations, Compared with Experimental Results^{40a}

	theory	experiment
a (Å)	4.741	4.737
c (Å)	3.193	3.186
u	0.306	0.307
E_g (eV)	2.95 (3.61)	3.62
ϵ_0^{\parallel}	9.47	9.58
ϵ_0^{\perp}	12.04	13.50

^aThe band gap from the GW calculation is given in parentheses.

upward both the valence band maximum (VBM) and CBM, by 0.17 and 0.83 eV, respectively. The band edge shifts result in a quasi-particle band gap of 3.61 eV, in excellent agreement with experiments. The static dielectric constants, which are needed for the image charge corrections,^{32,38} are calculated by the summation of the electronic part and the ionic part. At first, we calculate the electronic part (ion-clamped) macroscopic dielectric tensor, as well as the Born effective charges with the modern polarization theory.^{41,42} Then, the zone-center phonon frequencies were calculated with the finite differences scheme. Finally, the total dielectric matrix was obtained according to Cockayne and Burton,⁴³ and again reasonable agreement with the experiment has been obtained.

Electronic Structure of Group 15 Dopants in SnO_2 . The electronic structure of group 15-doped SnO_2 can be understood using the case of Bi-doping as a prototype. In Figure 3, we show the projected density of states (DOS) of Bi-s

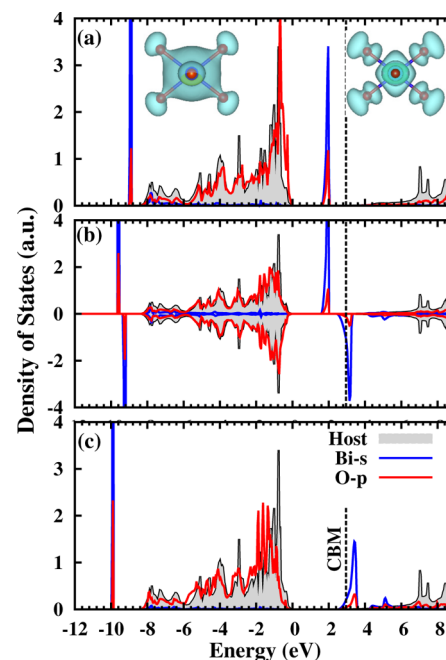


Figure 3. Projected density of states of Bi-s and O-p from the BiO_6 octahedron in Bi-doped SnO_2 with the defect charge states (a) $q = 1-$, (b) $q = 0$, and (c) $q = 1+$. The total density of states of the host is shown as a reference, the energy zero is set at the host VBM, and the host CBM is marked by the vertical dashed line. The charge density isosurface plots for both the bonding and antibonding states are shown in the insets. For $q = 0$, the densities of states in the majority and minority spin channel are plotted to positive and negative values, respectively.

states and O-p states from the oxygen ligands in the BiO_6 octahedron. It is seen that Bi-s and O-p states strongly couple with each other, forming an antibonding-like defect state inside the band gap and a bonding state about 9–10 eV below the VBM. In the insets in Figure 3a,⁴⁴ we show the charge density isosurface plots for these two states, illustrating their Bi-s/O-p character and the presence and absence of nodes at the bond center for the bonding and antibonding states, respectively.

As the charge state of the Bi_{Sn} defect increases from 1–, to 0, and then to 1+, the occupation number of the antibonding state decreases from 2, to 1, and then to 0. With the s electrons being released from the defect state, the chemical bonding becomes stronger, leading to a reduction of the (average) Bi–O bond length from 2.24 to 2.16 Å, and then to 2.07 Å. As seen in Figure 3, the decrease of the bond length is accompanied by an increase in the energy splitting between the bonding and antibonding states. The change of the bond length is also consistent with the decrease of the Bi ionic radii when the oxidation state increases from +3 to +5, and a similar change has been found in BaBiO_3 .⁴

Because of the nature of the antibonding state, the defect state near the CBM will rise in energy when the s–p coupling becomes stronger. The coupling strength is determined mainly by two factors, i.e., by the energy difference between the dopant atomic ns orbital and the oxygen 2p atomic orbital, and by the overlap integral, which depends on the bond length between the dopant and the ligands. In Figure 4, we show the atomic ns

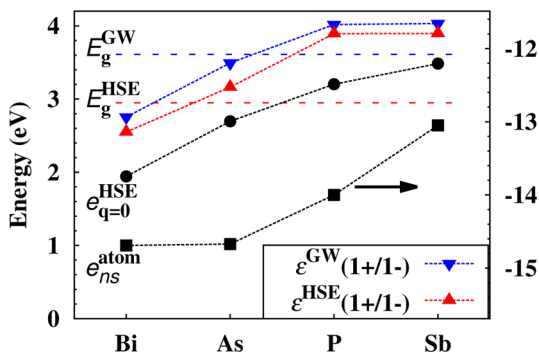


Figure 4. Atomic s orbital energy $e_{\text{ns}}^{\text{atom}}$ of the group 15 elements, the Brillouin-zone averaged single-particle energy level $\epsilon_{q=0}^{\text{HSE}}$, and the defect transition energy level $\epsilon(1+/1-)$ from both the HSE and GW approaches. The transition levels are given relative to the VBM of SnO_2 , and the band gap energy (position of the CBM) is indicated by the dashed lines.

orbital energy, $e_{\text{ns}}^{\text{atom}}$, as calculated within the scalar-relativistic local density approximation.⁴⁵ The atomic ns orbital energy does not increase with the atomic number but increases monotonically along the sequence of $\text{Bi} \rightarrow \text{As} \rightarrow \text{P} \rightarrow \text{Sb}$, which originates from the scalar relativistic effect as well as from the screening effects due to the fully occupied d- and f-shells. We further show in Figure 4, the Brillouin zone averaged single-particle energy of the antibonding defect state, $\epsilon_{q=0}^{\text{HSE}}$, and we indeed find this energy monotonically increases along the same sequence as the atomic ns orbital energy. Here, we have chosen to show the energy of the occupied single-particle defect state for $q = 0$. In the charge-neutral state, where the defect level is well-defined thanks to the constrained-DFT-like treatment described above. (Note that, except for the case of Bi, the empty defect state for $q = 1+$ is indistinguishable from the host conduction band.) Bi and As have comparable $e_{\text{ns}}^{\text{atom}}$ for their

valence s orbital; however, the s–p hybridization is much stronger in the case of As-doping, the energy splitting between the defect bonding and antibonding state is about 1 eV larger. We attribute this to the larger overlap integral between As-4s and O-2p, as implied by the about 0.2 Å shorter As–O bond than the Bi–O bond.

Structure Relaxation and the Negative- U Behavior of Group 15 Dopants in SnO_2 . As mentioned above for the case of Bi-doping, the BiO_6 octahedron contracts inward as the defect charge state increases from 1– to 1+ due to the strengthened chemical bonding. This behavior is observed for all dopants as shown in Table 2, where we give the average

Table 2. Calculated Average Bond Length (in Å) between the Dopant and Oxygen for Each Charge State and the Calculated U Value (in eV)^a

	P	As	Sb	Bi
$d_{q=1-}$	1.74; 2.45	2.09	2.23 ^b	2.24
$d_{q=0}$	1.74; 2.11	1.98	2.08	2.16
$d_{q=1+}$	1.78	1.88	2.00	2.07
U	−1.7	−0.8	−0.8	−0.3
U_e	+1.7	+1.3	+1.4	+1.3
U_r	−3.4	−2.1	−2.2	−1.6

^aFor each charge state, two numbers are given for P_{Sn} due to the asymmetric relaxation. The calculated U value is decomposed into the contributions from the direct electronic interaction (U_e) and from the ionic relaxation (U_r). ^bThe atomic configuration was obtained from a Hartree–Fock calculation (see text).

bond length for all charge states. The large change of the bond length of about 0.2 Å between the $q = 1-$ and the $q = 1+$ states results in a negative- U behavior. The U values calculated from eq 3 are −1.7, −0.8, −0.8, and −0.3 eV for P-, As-, Sb-, Bi-doping, respectively.

In order to analyze the origin of the negative- U behavior, we break the U values down into the contributions from the direct electronic (Coulomb) interaction (U_e) and from the ionic relaxation (U_r). Using the notations from Figure 2c, we have

$$U = U_e + U_r \quad (5)$$

$$U_e = E_1 - E_3 \quad (6)$$

$$U_r = 2E_2 - E_4 \quad (7)$$

Table 2 shows the decomposition of the U values. Overall, the electronic contributions, U_e , are quite similar for all dopants, but P_{Sn} has a somewhat larger Coulomb interaction due to the higher degree of localization of the P-s orbital. The large differences in the U values mainly come from the ionic relaxation part, which is strongly related to the ionic radius of the dopant. Basically, U_r increases as the ionic radius of the dopant increases, and Bi, which has the largest ionic radius, has the weakest negative- U behavior. An interesting symmetry breaking is observed for the $q = 1-$ and $q = 0$ states of P_{Sn} , which is the smallest defect atom (about 0.3 Å smaller radius than Sn). The PO_6 octahedron undergoes a C_3 distortion with three P–O bonds about 0.4–0.7 Å shorter than the other three P–O bonds. The charge density distribution resulting from the distortion resembles that of the lone-pair configuration in some Sn and Pb monoxides and monochalcogenides,^{46–48} i.e., the lone-pair points into the void formed by the three longer P–O bonds. Note that the lone-pair configuration only exists when a very strong cation-s–anion-p hybridization occurs, such as in

PbO, SnO, SnS, SnSe, and also here in P-doped SnO₂ but not in PbS, PbSe, PbTe, and SnTe.^{46–48}

Transition Levels and Electrical Activity of Group 15 Dopants in SnO₂. Because of the computationally confirmed negative-*U* behavior of the group 15 dopants, their electrical activity is determined by the position of the $\epsilon(1+/1-)$ transition level relative to the CBM, as anticipated in Figure 1. In Table 3, we give the relative position of this defect

Table 3. Calculated Transition Energy Level $\epsilon(1+/1-)$ (in eV) with Respect to the Host CBM for the Group 15 Dopants in SnO₂ from the Direct HSE06 Calculations and the HSE06+GW Calculations

	Bi	As	P	Sb
HSE06	−0.4	+0.2	+0.9	+0.9
HSE06+GW	−0.9	−0.1	+0.4	+0.4

transition energy level relative to the CBM as obtained from HSE06 and HSE06+GW calculations. As seen in Figure 4, the chemical trend of the defect transition level is similar to that of the atomic *ns* orbital energy. Bi_{Sn} has the deepest level, with $\epsilon(1+/1-)$ lying 0.9 eV below the CBM in the HSE06+GW approach. Thus, Bi-doping is expected to pin the Fermi level at this energy, thereby preventing the generation of free carriers. This finding confirms that the higher stability of Bi(III) is the origin of the conductivity reduction in Bi-doped SnO₂¹⁷ and explains why Bi-doping can be utilized to produce transparent high-resistivity SnO₂ thin films.¹⁸ Notably, a compensating +3 oxidation state has also been experimentally observed in Bi-doped β -PbO₂,¹⁹ which has an even higher propensity for *n*-type conduction than SnO₂. Further, it is interesting to compare the electronic transitions due to the +3 oxidation state of the group 15 dopants to those induced by the group 13 elements. In both cases, the electrical charge state ranges from 1− to 1+.^{49,50} In the present case of the group 15 dopants, considered for *n*-type doping, the $\epsilon(1+/1-)$ transition corresponds to an oxidation state change of the dopant atom itself, has negative-*U* character, and lies closer to the conduction band edge. In case of the group 13 dopants considered for *p*-type doping, the 1−, 0, and 1+ charge states correspond, respectively, to the ionized acceptor, to one hole bound at an oxygen ligand, and to two holes bound at two O ligands. Thus, these transitions result from the formation of a −1 oxidation state of one or two O ions. They have a positive-*U* character and lie closer to the valence band edge. However, there is no acceptor dopant that would have a small enough acceptor ionization energy, i.e., a $\epsilon(0/1-)$ transition close enough to the VBM to enable *p*-type doping with a significant free carrier density at room temperature.

Comparing the results of the combined HSE06+GW approach with the HSE06 result obtained within the standard defect supercell approach, we find that both approaches show the same trends, but a qualitative difference is found for the borderline case of As_{Sn}: in the direct HSE06 calculation, the $\epsilon(1+/1-)$ transition lies above the CBM, which would indicate that As is an active donor dopant but that it lies slightly below the CBM in HSE06+GW, which indicates a limitation of the doping efficiency of this dopant. Initially As will act as an electron donor and generate free electrons in the conduction band. However, as the Fermi level increases with the As dopant concentration, approaching the $\epsilon(1+/1-)$ transition level, part of the As dopants will change into the negatively charged (*q* =

1−) low valent +3 oxidation state, which acts as electron compensator. Hence, the electron charge carrier concentration of As-doped SnO₂ will eventually saturate. Notably, such limitation of the doping efficiency has been reported in a recent experimental literature.¹⁰ Both P and Sb dopants are found to have the $\epsilon(1+/1-)$ transition level well above the CBM, and the doping of SnO₂ should not be affected by the effect of multivalency in the case of these dopants. Indeed, there are experimental reports of electron concentrations up to 5×10^{19} and $1.7 \times 10^{21} \text{ cm}^{-3}$ that have been achieved with as the P- and Sb-doping, respectively.^{9,11} However, due to the large mismatch between the ionic radii of P and Sn, the P_{Sn} dopant has a rather high formation energy. Thus, the doping with P is probably limited by the formation of P₂O₅ secondary phases.^{7,9} Thus, Sb is the most favorable group 15 dopant in SnO₂ with the highest potential as a viable alternative to F-doping in SnO₂ based *n*-type TCO's.

CONCLUSIONS

We investigated theoretically the impact of the multivalency of group 15 dopants in SnO₂ on their electrical activity as *n*-type dopants for transparent conducting oxides. The determining factor is the energy difference between the conduction band minimum and the transition level at which the dopants change from the +5 into the +3 oxidation state. For an accurate prediction of this energy difference, we employed an approach that combines HSE06 hybrid functional calculations with GW quasi-particle energy calculations for both the band-edge energies and the defect state. Additionally, we described how constrained-DFT type calculations can be used to access the more unstable charge- and oxidation states. We discussed the chemical trends of the transition level and the negative-*U* behavior in terms of the dopant–ligand interaction as a function of atomic orbital energies and atomic radii. Bi_{Sn} shows a clear deep-level behavior with Fermi level pinning inside the band gap, thereby preventing doping and leading to insulating behavior. As_{Sn} is a borderline case, and only P_{Sn} and Sb_{Sn} act as electron donors without being affected by multivalency. Taking also the atomic size mismatch into account, we conclude that Sb is probably the only efficient *n*-type group 15 dopant in SnO₂.

AUTHOR INFORMATION

Corresponding Authors

*(H.P.) E-mail: Haowei.Peng@nrel.gov.

*(S.L.) E-mail: Stephan.Lany@nrel.gov.

Notes

The authors declare no competing financial interest.

ACKNOWLEDGMENTS

This work was supported by the U.S. Department of Energy, Office of Energy Efficiency and Renewable Energy, (SunShot initiative), under Contract No. DE-AC36-08GO28308 to NREL. The high performance computing resources of the National Energy Research Scientific Computing Center and of NREL's Computational Science Center are gratefully acknowledged.

REFERENCES

- (1) Emin, D. *Phys. Today* **1982**, 35, 34.
- (2) Stoneham, A. M. *J. Chem. Soc., Faraday Trans. 2* **1989**, 85, 505.
- (3) Peng, H.; Lany, S. *Phys. Rev. B* **2012**, 85, 201202.

- (4) Yan, B.; Jansen, M.; Felser, C. *Nat. Phys.* **2013**, *9*, 709–711.
- (5) Mizoguchi, H.; Kamiya, T.; Matsuishi, S.; Hosono, H. *Nat. Commun.* **2011**, *2*, 470.
- (6) Kykyneshi, R.; Zeng, J.; Cann, D. P. In *Handbook of Transparent Conductors*; Ginley, D. S., Hosono, H., Paine, D. C., Eds.; Springer, Berlin, Germany, 2010; Transparent Conducting Oxides Based on Tin Oxide; pp 171–191.
- (7) Varley, J.; Janotti, A.; Van de Walle, C. G. *Phys. Rev. B* **2010**, *81*, 245216.
- (8) Chopra, K. L.; Major, S.; Pandya, D. K. *Thin Solid Films* **1983**, *102*, 16.
- (9) Hsu, Y.-S.; Ghandhi, S. K. *J. Electrochem. Soc.* **1980**, *127*, 1595.
- (10) Dakhel, A. A. *Sol. Energy* **2012**, *86*, 126.
- (11) Kim, H.; Piqué, A. *Appl. Phys. Lett.* **2004**, *84*, 218.
- (12) Lee, S.-Y.; Park, B.-O. *Thin Solid Films* **2006**, *510*, 154–158.
- (13) Alsac, A. A.; Yildiz, A.; Serin, T.; Serin, N. *J. Appl. Phys.* **2013**, *113*, 063701.
- (14) Mao, W.; Xiong, B.; Liu, Y.; He, C. *Appl. Phys. Lett.* **2013**, *103*, 031915.
- (15) Tsuchiya, T.; Nakajima, T.; Shinoda, K. *Appl. Phys. B* **2013**, *113*, 333.
- (16) Li, C.; Li, J.; Li, S.-S.; Xia, J.-B.; Wei, S.-H. *Appl. Phys. Lett.* **2012**, *100*, 262109.
- (17) Rastomjee, C.; Dale, R.; Schaffer, R.; Jones, F.; Egdell, R.; Georgiadis, G.; Lee, M.; Tate, T.; Cao, L. *Thin Solid Films* **1996**, *279*, 98.
- (18) Foglietti, V.; Alessandro, A. D.; Galbato, A.; Alessandri, A.; Beccherelli, R.; Campoli, F.; Petrocco, S.; Wnek, M.; Maltese, P. *Mater. Res. Soc. Symp. Proc.* **1997**, *424*, 355.
- (19) Rothenberg, S.; Payne, D. J.; Bourlange, A.; Egdell, R. G. *J. Appl. Phys.* **2009**, *106*, 113717.
- (20) Birchall, T.; Bouchard, R. J.; Shannon, R. D. *Can. J. Chem.* **1973**, *51*, 2077.
- (21) Grzeta, B.; Tkalec, E.; Goebbert, C.; Takeda, M.; Takahashi, M.; Nomura, K.; Jaksic, M. *J. Phys. Chem. Solids* **2002**, *63*, 765–772.
- (22) Lili, L.; Liming, M.; Xuechen, D. *Mater. Res. Bull.* **2006**, *41*, 541.
- (23) Biswas, K.; Lany, S.; Zunger, A. *Appl. Phys. Lett.* **2010**, *96*, 201902.
- (24) Lany, S.; Zunger, A. *Phys. Rev. B* **2005**, *72*, 35215.
- (25) Anderson, P. W. *Phys. Rev. Lett.* **1975**, 953.
- (26) Alkauskas, A.; Broqvist, P.; Pasquarello, A. *Phys. Rev. Lett.* **2008**, *101*, 046405.
- (27) Becke, A. D. *J. Chem. Phys.* **1993**, *98*, 1372.
- (28) Perdew, J. P.; Ernzerhof, M.; Burke, K. *J. Chem. Phys.* **1996**, *105*, 9982.
- (29) Krukau, A. V.; Vydrov, O. A.; Izmaylov, A. F.; Scuseria, G. E. *J. Chem. Phys.* **2006**, *125*, 224106.
- (30) Peng, H.; Scanlon, D. O.; Stevanovic, V.; Vidal, J.; Watson, G. W.; Lany, S. *Phys. Rev. B* **2013**, *88*, 115201.
- (31) Rinke, P.; Janotti, A.; Scheffler, M.; Van de Walle, C. G. *Phys. Rev. Lett.* **2009**, *102*, 026402.
- (32) Lany, S.; Zunger, A. *Phys. Rev. B* **2010**, *81*, 113201.
- (33) Hedin, L. *Phys. Rev.* **1965**, *139*, A796–A823.
- (34) Blöchl, P. E. *Phys. Rev. B* **1994**, *50*, 17953.
- (35) Kresse, G.; Joubert, D. *Phys. Rev. B* **1999**, *59*, 1758.
- (36) Shishkin, M.; Kresse, G. *Phys. Rev. B* **2006**, *74*, 035101.
- (37) Shishkin, M.; Kresse, G. *Phys. Rev. B* **2007**, *75*, 235102.
- (38) Lany, S.; Zunger, A. *Phys. Rev. B* **2008**, *78*, 235104.
- (39) Wu, Q.; Van Voorhis, T. *Phys. Rev. A* **2005**, *72*, 024502.
- (40) Madelung, O. *Semiconductors: Data Handbook*; Springer, Berlin, Germany, 2003.
- (41) King-Smith, R.; Vanderbilt, D. *Phys. Rev. B* **1993**, *47*, 1651.
- (42) Vanderbilt, D.; King-Smith, R. *Phys. Rev. B* **1993**, *48*, 4442.
- (43) Cockayne, E.; Burton, B. *Phys. Rev. B* **2000**, *62*, 3735.
- (44) Momma, K.; Izumi, F. *J. Appl. Crystallogr.* **2011**, *44*, 1272.
- (45) Kotochigova, S.; Levine, Z. H.; Shirley, E. L.; Stiles, M. D.; Clark, C. W. *Phys. Rev. A* **1997**, *55*, 191.
- (46) Walsh, A.; Payne, D. J.; Egdell, R. G.; Watson, G. W. *Chem. Soc. Rev.* **2011**, *40*, 4455.
- (47) Walsh, A.; Watson, G. J. *Phys. Chem. B* **2005**, *109*, 18868.
- (48) Walsh, A.; Watson, G. W. *J. Solid State Chem.* **2005**, *178*, 1422.
- (49) Scanlon, D. O.; Watson, G. W. *J. Mater. Chem.* **2012**, *22*, 25236.
- (50) Lany, S.; Zunger, A. *Phys. Rev. B* **2009**, *80*, 085202.